

Phaser: Enabling Phased Array Signal Processing on Commodity WiFi Access Points

Jon Gjengset, Jie Xiong, Graeme McPhillips, Kyle Jamieson
Department of Computer Science, University College London
{j.gjengset, j.xiong, g.mcphillips, k.jamieson}@cs.ucl.ac.uk

ABSTRACT

Signal processing on antenna arrays has received much recent attention in the mobile and wireless networking research communities, with array signal processing approaches addressing the problems of human movement detection, indoor mobile device localization, and wireless network security. However, there are two important challenges inherent in the design of these systems that must be overcome if they are to be of practical use on commodity hardware. First, phase differences between the radio oscillators behind each antenna can make readings unusable, and so must be corrected in order for most techniques to yield high-fidelity results. Second, while the number of antennas on commodity access points is usually limited, most array processing increases in fidelity with more antennas. These issues work in synergistic opposition to array processing: without phase offset correction, no phase-difference array processing is possible, and with fewer antennas, automatic correction of these phase offsets becomes even more challenging. We present Phaser, a system that solves these intertwined problems to make phased array signal processing truly practical on the many WiFi access points deployed in the real world. Our experimental results on three- and five-antenna 802.11-based hardware show that 802.11 NICs can be calibrated and synchronized to a 20° median phase error, enabling inexpensive deployment of numerous phase-difference based spectral analysis techniques previously only available on costly, special-purpose hardware.

Categories and Subject Descriptors

C.3 [Special-purpose and application-based systems]: Signal processing systems

Keywords

Phased-array; Signal processing; NICs synchronization; Phase calibration; Angle-of-arrival; Location tracking

1. INTRODUCTION

In recent years, there has been renewed interest within the mobile and wireless networking communities in addressing problems re-

Permission to make digital or hard copies of part or all of this work for personal or classroom use is granted without fee provided that copies are not made or distributed for profit or commercial advantage, and that copies bear this notice and the full citation on the first page. Copyrights for third-party components of this work must be honored. For all other uses, contact the owner/author(s). Copyright is held by the author/owner(s).

MobiCom'14, September 7-11, 2014, Maui, Hawaii, USA.

ACM 978-1-4503-2783-1/14/09.

<http://dx.doi.org/10.1145/2639108.2639139>.

lated to the sensing of signals using multi-antenna (MIMO) access points. Recent examples include systems that localize RFID tags [27] and WiFi devices [22, 30], enhance WiFi security [31], and passive radar systems that pinpoint human movements [1, 2, 17].

These systems, and others, share an important common thread: they all rely on phased array signal processing; a set of techniques that makes various comparisons between the radio signals received from each of the antennas of the access point (AP). Phased array processing has been applied in weather and military radar, seismology, and astronomy to great benefit, but its application to indoor and outdoor wireless and mobile communications presents new challenges and dictates novel system designs, as the above work demonstrates.

While the aforementioned work makes phased array signal processing practical in mobile wireless local-area network designs, two important challenges remain that must be overcome if it is to be widely deployed on off-the-shelf hardware:

1. On a single commodity wireless NIC, the RF oscillators are frequency locked, preventing their relative phases from drifting over time. However, these oscillators still have an unknown, absolute phase offset relative to one another. This offset must be compensated for in order to obtain readings from an AP that have meaning in physical space.
2. Today's cutting-edge APs are equipped with multiple unsynchronized network interface cards (NICs), each with multiple antennas [32], but phased-array signal processing benefits most from phase difference readings between all pairs of antennas, whether they share a radio card or not. The complete lack of synchronization across NICs in both time and radio frequency stymies attempts to run the above systems across multiple NICs at the same AP.

In this paper, we present *Phaser*; a system that enables phased array signal processing for commodity WiFi APs. We also propose minor, cost-effective hardware modifications that can further improve the phase-data fidelity on such APs. WiFi today is ubiquitous, with APs deployed everywhere people congregate. Phaser's vision is to convert every one of these APs into a miniature phased array receiver, so that when integrated with Phaser, the above systems can truly run pervasively—everywhere WiFi APs are deployed.

To realize this vision, Phaser addresses these challenges with three corresponding wireless system components that we implement at a backend server connected to the APs over Ethernet backhaul:

First, novel software-based digital signal processing on the general-purpose CPU of the backend server works alongside an inexpensive custom antenna design at the AP to enable multiple commodity NICs to be synchronized in time and frequency, and form a larger and more useful phased array.

Second, Phaser introduces a novel phase *autocalibration* algorithm that corrects the phase offsets between the different radio

oscillators at an AP. Our autocalibration algorithm operates without the need for human interaction, and works in the presence of noise and indoor multipath reflections.¹

Finally, Phaser leverages signal onset detection to reduce the effects of multipath reflections, yielding significantly improved end-to-end performance.

We observe that the system’s components require only the addition of software-based digital signal processing on a general-purpose CPU, and for multicard operation, the addition of custom-designed, yet simple and inexpensive hardware: RF switches, splitters and antennas with known geometries. Most of the computational load is performed by a server connected to the Ethernet backhaul, further reducing the changes needed on the APs. We therefore position Phaser as a likely design pattern for future 802.11 AP hardware designs that is compatible with the MIMO designs in 802.11n and upcoming MU-MIMO designs in 802.11ac.

Contributions. To summarize, this paper makes the following three research contributions:

1. We introduce a multicard synchronization algorithm and design that allows multiple NICs to take phase-difference readings as if they were one large antenna array.
2. We propose an autocalibration algorithm so APs may calibrate their antennas automatically—even across multiple NICs—based on transmissions from other clients or APs.
3. We further integrate the above two ideas with a multipath suppression algorithm, which significantly reduces the impact of multipath on Phaser’s performance.

Non-goals. Phaser aims to enable phased signal processing on commodity hardware, and does so by correcting for a number of factors that introduce phase errors into the readings reported by an AP’s NICs. While there are many other digital communication techniques in use in the wireless community that are also based on wireless phase data, the particularities of Phaser make it unsuitable for use with some of these. Specifically, Phaser is not meant to be used to synchronize MIMO transmissions, nor does it enable improved packet reception or decoding. The attentive reader will realize that Phaser’s phase difference accuracy and multi-card synchronization are simply not of sufficiently high fidelity for these applications.

Paper roadmap. The rest of this paper is organized as follows: we begin with a detailed description of Phaser’s design (§2), followed by details of our implementation on commodity Intel 5300 NIC hardware, combined with a custom, low-cost antenna hardware circuit design (§3). Our experimental evaluation (§4) measures the quality of the Phaser AP improvements both in isolation in an anechoic chamber and in end-to-end operation in an office environment. Results show that Phaser can resolve multipath reflections using multiple NICs to a $\pm 2^\circ$ accuracy, and automatically calibrate APs in a busy office environment to an average accuracy of 20° phase error, yielding qualitatively similar angle-of-arrival information to that of expensive, specialized hardware built for phased array processing. We also report improvements in calibration, and a significant (35%) improvement in median accuracy for a location system running on top of Phaser due to multipath suppression alone. We cover related work in §5 and conclude in §6.

2. DESIGN

In this section, we discuss the main components of Phaser that allow accurate phase-difference readings to be extracted from commodity RF hardware. We first describe the theory of multicard operation

¹N.B.: this phase calibration is conceptually distinct from the “calibration” or “war-driving” that some indoor location systems require, involving a human taking readings within an indoor space.

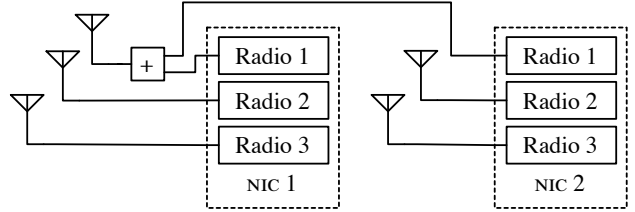


Figure 1: Phaser’s multi-radio hardware design for the case of two NICs. The design generalizes to any number of NICs, each sharing one antenna from their first radio.

in §2.1. In §2.2, we tackle the problem of automatic detection of radio-chain phase offsets, and in §2.3, we describe an optimization that reduces the detrimental effects of multipath signals.

2.1 Multicard operation

On a single NIC, phase data from each antenna can be compared after compensating for the phase offsets introduced by each of the radio chain oscillators as described in §2.2. However, across radios, many other factors distort the OFDM signal, and each of these varies slightly between the two NICs:

1. The sampling frequency f_s , with which the RF front end samples the incoming signal in the time domain.
2. The carrier frequency f_c to which the RF front end is tuned.
3. The RF sample clock time offset τ , measured in time samples relative to the beginning of an OFDM symbol. This varies because the two NICs detect and acquire the incoming frame at slightly different points in time.
4. RF oscillator phase offset ϕ . As noted above, this varies between antennas on one NIC because it is locked to a random but constant value at power-up. It varies between antennas on different NICs because the two NICs’ RF oscillators are not frequency-locked.

To further complicate matters, all the above quantities vary on a frame-by-frame basis, so any correction algorithm must be able to work at line rate as frames arrive from the NIC. In this section, we present a hardware design and a synchronization algorithm that lets us compensate for these differences, and thereby enable phase-difference signal processing across antennas on multiple NICs as if they were phase-locked.

2.1.1 Hardware design

To achieve higher antenna counts, Phaser augments an AP’s NIC with one or more receive-only NICs, operating on the same channel. Phaser splits the incoming signal from one antenna and routes it to one radio chain on both NICs, as shown in Figure 1. This allows one radio chain on each NIC to receive a signal that we know is equal (as viewed at the antenna) to that which a radio chain on the primary NIC received, but sacrifices one antenna that may otherwise be used for spatial multiplexing. While this is unfortunate, we believe this is a reasonable trade-off for deployments where the opportunities provided by phased signal processing outweigh the need for increased throughput. The result is a five-antenna AP, but the raw CSI² readings from the two unsynchronized NICs cannot be combined for phased array processing without compensating for the aforementioned inter-NIC irregularities.

²The WiFi standards refer to the channel readings that arrive with each received frame as *channel state information* or CSI. CSI readings are primarily used for channel estimation, but also contain the phase information that phased-array signal processing techniques require. We refer to phase information and CSI interchangeably throughout this paper.

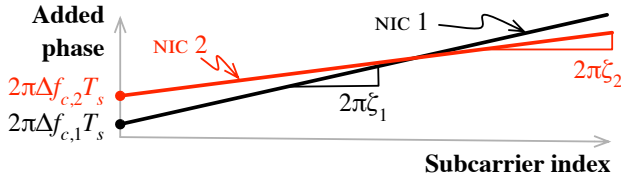


Figure 2: Phase added to a CSI measurement of an OFDM reception due to transmitter-receiver carrier frequency differences $\Delta f_{c,1}$, $\Delta f_{c,2}$ and the respective sampling frequency differences ζ_1 , ζ_2 between the transmitter and each of the receiving NICs.

2.1.2 Software synchronization algorithm

Upon receiving CSI from each NIC, we first isolate the readings from the shared antenna introduced above. We then arbitrarily, but consistently across packets, select one NIC as the *primary*. For the purposes of discussion, we refer to the frequency-domain CSI of the primary and secondary NIC as $H_1[k]$ and $H_2[k]$, respectively. We now seek a transformation of $H_2[k]$ so that readings for the shared antenna on that NIC matches the readings taken by the primary. We know such a transformation must exist since the two NICs have observed the same signal at the same antenna.

Synchronizing carrier and sampling frequency. We first reconcile f_c and f_s between the two NICs. A difference in f_c between an OFDM sender and receiver manifests as an added phase in H_2 whose magnitude is constant across subcarriers [25]. Suppose the difference in f_c between the sender and NIC 1 is $\Delta f_{c,1}$, and the difference in f_c between sender and NIC 2 is $\Delta f_{c,2}$. The two NICs will experience added phases whose y-intercepts are as shown in Figure 2.

Furthermore, if the sender transmits with a sampling frequency of f'_s , then the fractional difference in sampling frequency between sender and NIC 1 is $\zeta_1 = \frac{f_{s,1}}{f'_s} - 1$, with an analogous definition for NIC 2. This manifests as an added phase whose magnitude varies linearly across subcarriers [25] with slopes $2\pi\zeta_1$ and $2\pi\zeta_2$ for NICs 1 and 2, respectively, as shown in Figure 2.

We correct for both carrier and sampling frequency differences by setting the angle of each complex sample from the second card to the angle of the corresponding sample from the primary card while leaving the magnitudes untouched. In the frequency domain, this rotates $H_2[k]$ by the difference between the two curves shown in Figure 2, creating a new CSI for NIC 2 with a constant phase shift of $\gamma = 2\pi(\Delta f_{c,2} - \Delta f_{c,1})T_s$ and a phase shift linear in frequency of slope $\alpha = 2\pi(\zeta_2 - \zeta_1)$:

$$H'_2[k] = H_2[k]e^{j(\gamma + \alpha k)}. \quad (1)$$

This transformation is valid since we know that the received signals for both NICs were equal at the shared antenna.

Synchronizing sample clocks. Due to multipath effects, two NICs also acquire an incoming transmission at slightly different points in time, causing a shift τ in the time-domain samples. To see the effect this has on the CSI, let us examine the Discrete Fourier Transform of NIC 2's CSI:

$$H_2[k] = \sum_{n=0}^{N-1} h_2[n]e^{-j2\pi kn/N}. \quad (2)$$

If we circularly shift $h_2[n]$ in time by a whole number of samples, it can be shown that the effect in the frequency domain is again a phase shift linear in frequency:

$$H_2[k]e^{2\pi j\tau_0 k/N} = \sum_{n=0}^{N-1} h_2[(n - \tau_0)_N]e^{-j2\pi kn/N}. \quad (3)$$

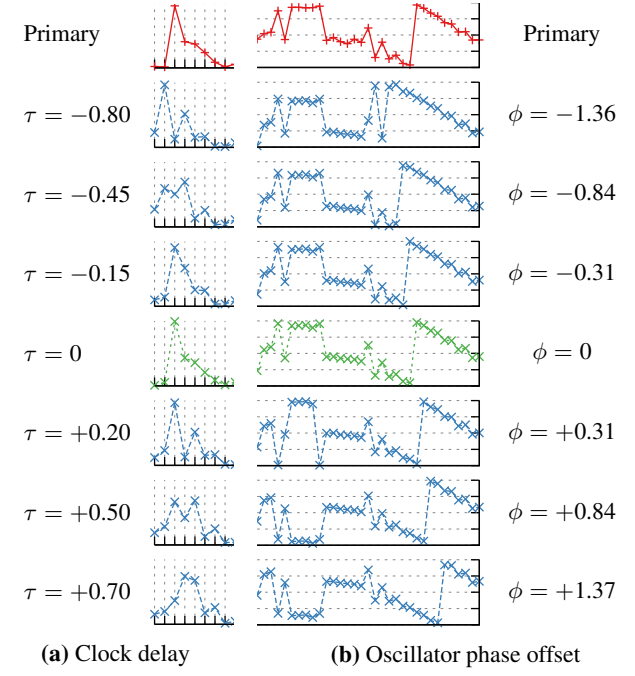


Figure 3: Magnitude (a) and phase (b) for consecutive time-domain samples from NIC 1 and NIC 2 with different Phaser search parameters after compensating for f_c and f_s .

Comparing the right-hand-side of Equation 1 with the left-hand-side of Equation 3 we see that the carrier and sampling frequency synchronization step also corrects such time shifts.

This shift will in practice be *less* than one sample period in magnitude. Nonetheless, it can also be shown that a linear phase shift in frequency whose slope is fractional approximates a filter that shifts the sampled signal $h_2[n]$ by reconstructing the underlying continuous signal and resampling that fractional number of samples later in time [13]. The upshot of this is that our carrier and sampling frequency synchronization step also synchronizes the two NICs in time even down to a fraction of a time sample.

Figure 3(a) shows the shared antenna signal from the primary NIC (uppermost plot) and from another NIC, with varying fractional delays applied (remaining plots) after f_c and f_s have been compensated for. We see that the frequency-domain transformation has temporally aligned the two signals. Note that for the longer fractional delay, the peak falls between two samples, and thus becomes obscured.

Correcting oscillator phase offset. The absolute phase measured by the radio chains connected to the shared antenna on each card varies, as their oscillators have different phases. More importantly, the two vary continuously and independently of each other, and can thus not simply be measured once like the inter-antenna phase offsets on a single NIC with frequency-locked oscillators discussed in §2.2. In order to give the appearance that the oscillators from the two NICs are all phase-locked³, our synchronization algorithm must therefore also cancel out this unpredictable phase offset.

This phase offset manifests as a phase rotation of every time-domain sample. Again, however, consider the right-hand-side of Equation 1. By adjusting γ to equalize phase in the frequency domain, we do the same in the time domain, and so align the phase

³If two oscillators are phase-locked, their absolute phase difference is constant over time.

of the primary NIC's signal with the secondary's, as shown in Figure 3(b).

To complete the synchronization, we apply the correction $e^{j(\gamma+\alpha k)}$ from Equation 1 to the samples from all the other antennas on the non-primary NIC. We also multiply the magnitude of the time-domain samples taken from the shared antenna by the number of cards present in order to counter loss introduced by the splitter. This gives us a set of readings that can be treated as phase-locked, despite being from different cards. We note that this synchronization algorithm also compensates for any differences in phase caused by slightly different cable lengths to the shared antenna for the two cards, or by phase unbalance in the splitter, as these are subsumed by the constant phase shift γ of Equation 1.

2.1.3 Interchannel interference

The astute reader will observe that the carrier frequency offset (CFO) and the sampling frequency offset (SFO) both introduce intercarrier interference (ICI), which contributes additional noise to the received signal. If this noise is too large, it would break Phaser's assumption that the phase offset between the shared antenna on two cards is the same for any other pair of antennas, causing multicard synchronization to fail.

The relationship between ICI and SFO, CFO and other factors such as transmitter movement is well understood [9], and both theoretical and experimental results show that the power of ICI caused by SFO is usually several orders of magnitude smaller than the power of the received signal. The 802.11 specification requires conforming sampling clocks to be accurate to 20 ppm, giving an ICI that is 80 dB weaker than the power of the original signal. For Phaser, this means that SFO-induced ICI can safely be considered negligible noise.

CFO on the other hand can introduce ICI that greatly distorts the received signal, and could thus introduce a significant error term in Phaser. However, given the short timescale of the 802.11 preamble over which the CSI is computed, the coarse and fine Schmidl-Cox synchronization performed by 802.11 OFDM receivers effectively eliminates the CFO between the sender and the receiver. The near-zero remaining CFO causes no noteworthy ICI, and thus can also be safely ignored.

2.2 Autocalibration

Since each radio chain connects to a different RF oscillator, their absolute phases differ despite being frequency-locked. In order to obtain useful phase-difference data, array processing systems must eliminate these constant phase differences. While these could be measured by splitting a reference signal along carefully-measured cables [30], or by transmitting a known signal from one antenna to the other antennas on the same AP [24], these approaches interrupt normal communication, and become disruptive if multiple devices have to be calibrated, or if devices restart and require recalibration.

In this section, we propose a technique for automatically calibrating an AP \mathcal{A} that has just been powered up. We present our method in three stages: first, at the lower level, we present a metric, *η -scoring*, for evaluating the degree of correspondence between a pseudospectrum and a given bearing (§2.2.1). Then we present a technique for determining likely candidate phase offsets from a single transmission (§2.2.2). Finally, we give the full algorithm, which uses η -scoring, cross-packet calibration and a “reset” mechanism to achieve resilience against multipath RF propagation (§2.2.3).

Requirements. The only information autocalibration needs is the locations of the APs and potentially other transmitters in the system; for APs, these are assumed to be entered by the sysadmin who installs the AP into Phaser's database, but Phaser can also use transmissions from clients whose position is determined by a localization system.

Metric (η -score):

1. Find a normalizing constant k such that $\int k\mathcal{P}(\theta) d\theta$ is one, and set $\mathcal{P}' = k\mathcal{P}$.
2. Construct a Gaussian mask $g_\alpha(\theta)$ with an expected value α and a variance according to the desired level of error tolerance. Set $\bar{g}_\alpha(\theta) = 1 - g_\alpha(\theta)$.
3. Calculate $\eta(\mathcal{P}, \alpha) = \frac{\int g_\alpha(\theta)\mathcal{P}'(\theta) d\theta}{\int \bar{g}_\alpha(\theta)\mathcal{P}'(\theta) d\theta}$.

Figure 4: Scoring a pseudospectrum \mathcal{P} arising from a trial combination of phase offsets against a bearing to the AP α . The output of this calculation, the η -score, feeds into the overall autocalibration algorithm.

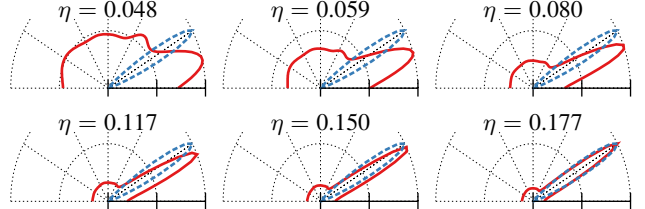


Figure 5: η -scoring different phase combinations that yield various pseudospectra (solid red curves) with energy directed towards and away from the true bearing (broken blue curve).

2.2.1 Scoring individual frames

When CSI for a frame arrives at the autocalibrating AP \mathcal{A} , we use spectral techniques on phase-difference readings from the CSI to construct an angle-of-arrival *pseudospectrum* [20]; an estimate of the power of the incoming signal versus bearing to the AP. Since we know the location of the transmitter and the receiver, we have a relatively accurate estimate of the direct-path bearing $\hat{\alpha}$, and thus we know in which direction we are likely to sense energy. As the phase difference, and hence the pseudospectrum, changes with different oscillator phase offsets, we are able to use Phaser's η -scoring metric to find a set of phase offsets that produce a pseudospectrum with energy directed toward $\hat{\alpha}$. The careful reader will note that when an obstruction blocks the direct path to \mathcal{A} , this approach in isolation will miss the direct path and score a reflected path highly. We rely on the “outer loop” of the autocalibration algorithm (§2.2.3) to overcome this challenge.

To determine the extent to which a pseudospectrum \mathcal{P} matches $\hat{\alpha}$, we seek a metric that increases in the presence of peaks towards bearing $\hat{\alpha}$, and decreases in the presence of peaks at bearings away from $\hat{\alpha}$. Since $\hat{\alpha}$ is an estimate, we also want the metric to be continuous with respect to bearing, so that \mathcal{P} 's peak does not have to *exactly* coincide with $\hat{\alpha}$.

By comparing the area under \mathcal{P} in the vicinity of AP bearing α with the area under \mathcal{P} toward all other bearings, the *η -score* $\eta(\mathcal{P}, \alpha)$ shown in Figure 4 fulfills the above goals. Peaks in directions away from α , or a high noise floor, increase the denominator in Step 3, thus decreasing $\eta(\mathcal{P}, \alpha)$. Figure 5 shows η for six different combinations of phase offsets for a linear three-antenna array. As desired, the η -score is highest when a peak is present in the direction of $\hat{\alpha}$, and lower when there are peaks elsewhere.

The Gaussian ensures that pseudospectra with peaks close to α also get high η -scores, thus tolerating inaccuracies in the estimation of α . The width of the Gaussian should be chosen such that it matches the width of a peak in a pseudospectrum with most power directed toward the signal's true bearing. With increasing number

of antennas, peaks get sharper, and thus the variance of the smoothing function should be decreased. For arrays with relatively few antennas, an experimental sensitivity analysis (§4.2.2) shows that a Gaussian with variance $\sigma^2 = 0.1$ works well.

2.2.2 Autocalibration algorithm

Upon receiving CSI from a frame⁴ at \mathcal{A} , an N -antenna AP, we need to explore the $N - 1$ -dimensional phase offset space, but an exhaustive search of all phase offset combinations on each received transmission would be very expensive for large N . To make this operation tractable, we observe that an N -antenna array can be viewed as a number of smaller and overlapping L -antenna subarrays.

We begin with the algorithm for each L -antenna subarray \mathcal{A}_i . This maintains a *current best set* of phase offsets \mathcal{B}_i , which starts out empty. Each candidate E in \mathcal{B}_i consists of a set of $L - 1$ phase offsets $\phi_1^E, \dots, \phi_{L-1}^E$ along with the η -score of the pseudospectrum resulting from applying those phase offsets to the frame's received CSI. We now consider every combination of the $L - 1$ possible phase offsets with a *phase granularity* $\Delta\phi$ a candidate for insertion into \mathcal{B}_i . Given a candidate C , we now need to decide whether C should be inserted into \mathcal{B}_i , and if so, which element to evict from \mathcal{B}_i once it grows beyond a certain *candidate population size* S . We explore the effect of varying S and $\Delta\phi$ in §4.2.

We aim for each \mathcal{B}_i to contain phase offset combinations that yield good η -scores, while still maintaining diversity so that if the ground-truth correct phase offset has a lower η -score, it will not be completely disappear from \mathcal{B} . To achieve this, we compare C with a randomly-selected $E \in \mathcal{B}$ and probabilistically replace E by C based on two ratios. The first, $\Delta\eta = \eta_C / \eta_E$, measures how much better C 's η -score is than E 's. The second ratio captures the impact of replacing E by C on diversity. We compute

$$\sigma_{\mathcal{B}_i}^2 = \sum_{k=1}^{L-1} \sum_{E \in \mathcal{B}_i} \left(\phi_k^E - \bar{\phi}_k \right)^2 \quad (4)$$

where $\bar{\phi}_k$ is the average phase offset for antenna pair k in \mathcal{B}_i . Then we compare $\sigma_{\mathcal{B}_i}^2$ with $\sigma_{\mathcal{B}_i \setminus \{E\} \cup \{C\}}^2$ by the ratio

$$\Delta\sigma_{CE}^2 = \sigma_{\mathcal{B}_i \setminus \{E\} \cup \{C\}}^2 / \sigma_{\mathcal{B}_i}^2. \quad (5)$$

The two ratios $\Delta\eta$ and $\Delta\sigma_{CE}^2$ give us information about how much better or worse C is than E . To determine the probability of replacement, $p_r(C, E)$, we first observe that, as the population stabilizes, $\Delta\eta$ and $\Delta\sigma_{CE}^2$ will generally be very close to one. We therefore want to increase $p_r(C, E)$'s sensitivity when the ratios are close to one, and cap it such that we discard obviously poor ratios and keep obviously good ratios. This can be achieved by applying a shifted exponential function to each ratio as shown in Equation 6:

$$p_r(C, E) = a \left(b^{\Delta\eta-1} / 2 + b^{\Delta\sigma_{CE}^2-1} / 2 - c \right) + 1/2. \quad (6)$$

By choosing a and b , we can adjust the sensitivity of the probability to small changes in $\Delta\eta$ or $\Delta\sigma^2$ when the ratios are close to one. We pick c to center the distribution at zero, meaning c is uniquely determined by the choice of a and b . By adding $1/2$ to p_r , we normalize $p_r(C, E) = 0.5$ when C and E are equally good candidates.

The choice of a and b will depend upon the expected variation in $\Delta\eta$ and $\Delta\sigma^2$. While the expected variation in $\Delta\sigma^2$ is unpredictable across transmissions, and thus cannot be tuned for specifically, the variation in $\Delta\eta$ will vary depending on the array geometry, because different antenna geometries may produce different distributions of

⁴Possibly from multiple cards and combined as explained in §2.1.

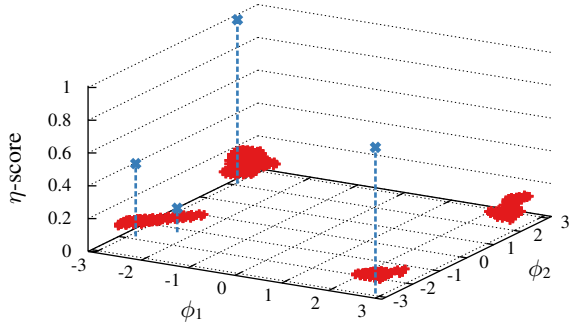


Figure 6: Phaser's cross-packet calibration clustering algorithm operating with packets from four different APs.

η scores as combinations of ϕ are searched. We have found that for a five-antenna uniformly linear array, $a = 10$, $b = 2.718$ and $c = 1$ yields good diversity in the population while still maintaining high η -scores across several deployments.

After this selection, we have $N/(L - 1)$ populations, each containing the best candidates for one sub-array. We can now generate candidates for \mathcal{B} , the final population, by picking one candidate from each population, $c_i \in \mathcal{B}_i$, and subtracting the phase offset of the overlapping antenna in c_0 from all phase offsets in each c_i . The resulting candidate is probabilistically inserted into \mathcal{B} in the same way as for each \mathcal{B}_i .

2.2.3 Multi-packet operation

After this process completes, \mathcal{B} contains a diverse set of phase offset combinations⁵ that all yield high η -scores. We reduce this to a single combination with the observation that across frames from different transmitters, combinations close to the ground-truth phase offsets E^* appear in almost every population \mathcal{B} , and phase offsets due to multipath reflections vary randomly across populations from different transmitters. To exploit this, we introduce a *cross-packet population*, Ψ , into which all elements of each \mathcal{B}^k (the final candidate phase offset set for received frame k) are placed such that $\Psi = \mathcal{B}^1 \cup \dots \cup \mathcal{B}^K$ across K received packets. Then we apply standard clustering algorithms to Ψ , where the distance between two samples is determined by the unwrapped Euclidean distance of the phase offsets and the sample's η -score. Figure 6 shows the result of performing this clustering on a three-antenna array across 50 packets received from three transmitters.

To estimate the correct phase offset combination, we now find the cluster with the highest product of number of samples and average η -score, and the parameters of its centroid are used as the true phase offset combination. This metric dictates the height of the dotted line going through each identified centroid in the figure. This ordering rewards phase combinations that consistently give pseudospectra that have good correlation with the true angle of arrival (AoA).

2.2.4 Practical considerations for autocalibration

AP placement estimation error. Autocalibration only has an estimate of the bearings of incoming signals. Because of this, the η -score will not reach a maximum for the true combination of phase

⁵Several phase combinations can yield peaks toward a given bearing depending on the multipath environment and the antenna geometry.

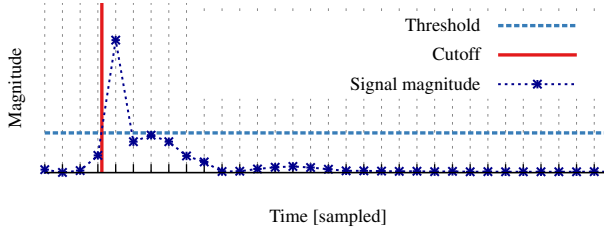


Figure 7: Magnitude of sampled time-domain signal showing line-of-sight arrival and multipath arrivals. Horizontal line indicates onset threshold, vertical line indicates cutoff point after upsampling.

offsets as the peak of the pseudospectrum for the true phase offsets will no longer align with the bearing that autocalibration is attempting to maximize against.

To counter this problem, we add another dimension to the search in each L -antenna sub-array. For each phase offset combination, we calculate the η -score for several smaller rotations of the normalized pseudospectrum \mathcal{P}' . Since we assume that the system knows the rotation and location fairly accurately, only a very narrow range of rotations ($\pm 5^\circ$) need to be searched. Due to the Gaussian smoothing, we can also search quite coarsely, as even an approximate match will receive a higher η -score. When performing probabilistic insertion, we now also consider the rotation that was used in conjunction with the phase offsets we are iterating on top of. Since a rotation of \mathcal{P}' is computationally trivial, recalculating the η -score for a small number of rotations is a sufficiently inexpensive operation that it does not significantly impact the running time of the autocalibration algorithm.

Calibration reset. Occasionally, this algorithm may yield incorrect phase offsets, causing an AP to be miscalibrated. Once autocalibration has terminated, the AP participates in a larger, multi-AP system along with other nearby APs. Suppose this system is a location tracking system and estimates a client’s location as \mathbf{x} . The calibrated AP \mathcal{A} measures the degree to which it agrees with that location by evaluating its pseudospectrum at the bearing corresponding to \mathbf{x} , $\theta_{\mathbf{x}}$. If \mathcal{A} consistently disagrees with the location system’s estimate across many clients, it is likely that \mathcal{A} has been miscalibrated. Phaser thus resets the calibration and reruns autocalibration. This alleviates the event that a burst of packets from a far-away AP or client miscalibrates \mathcal{A} .

2.3 Onset detection

Real-world wireless environments are replete with walls and other objects that reflect wireless signals, causing multipath reflections that complicate angle-of-arrival computations significantly. These additional signals can significantly reduce the fidelity of the pseudospectra, particularly for antenna-constrained arrays.

To address this, Phaser uses a simple, yet effective optimization that allows it to suppress a large portion of the multipath power in an incoming signal. Consider the magnitude of an incoming signal over time shown in Figure 7. There is typically a clear peak for the line-of-sight (LOS) arrival, and then later peaks and bumps for the arriving reflected signals. This observation matches what we know of the fundamentals of physics; reflected signals must necessarily arrive at a strictly later point in time than the LOS signals.

We use this insight to suppress the multipath arrivals: we apply a peak detection algorithm to the received signal’s magnitude, identify the first peak, and eliminate any samples appearing after that peak when doing spectral analysis of the signal. Since we are looking at a sampled signal, this technique cannot eliminate multipath sig-

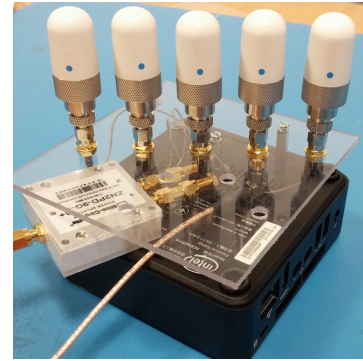


Figure 8: The 5-antenna Phaser AP with one antenna shared by both NICs. The signal from this shared antenna is split and fed into one RF front end on each NICs.



Figure 9: The inside of Phaser AP with one Intel 5300 card shown. Two NICs are employed to have a total of six available RF chains.

nals that arrive within the same sampling period as the LOS arrival. However, as we show experimentally in §4.3, the effect of removing even some of the multipath signals is substantial.

We also observe that the incoming signal can be upsampled by using a higher number of samples in the inverse Fourier Transform applied to the frequency-domain in the CSI. This increased resolution allows us to further improve multipath suppression; instead of removing any samples after the LOS peak, we eliminate all samples after the *onset* of this peak. While this will reduce the gain of the LOS signal, it will also significantly reduce the impact of multipath transmissions that fall within the same sample period. Figure 7 shows the cutoff point for a received signal using a third of the signal’s min-max span as the onset detection threshold. This optimization is further evaluated in §4.3.

3. IMPLEMENTATION

We have implemented Phaser on *Intel Next Unit of Computing* devices with *Intel Wireless Link 5300 802.11n MIMO* NICs as shown in Figure 8 and 9. Using this commodity hardware, we have access to 802.11 CSI readings [10], which enables us to extract per-subcarrier phase information. Because of firmware limitations, we were only able to get reliable phase readings at 5 GHz. Antennas are spaced at a half-wavelength distance (2.68 cm) in a linear form to yield maximum AoA spectrum resolution which is also the arrangement preferred in commodity APs. As shown in Figure 8, a splitter is employed to feed the signal received from the shared antenna to both of the NICs for synchronization purpose.

System data flow. The APs are set up in promiscuous wireless monitoring mode, and forward all 802.11 headers and CSI readings

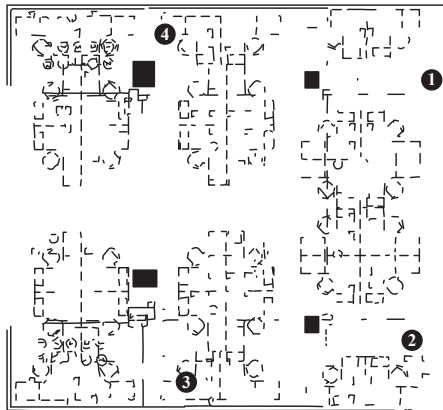


Figure 10: Map of the office environment used for the following experimental evaluation. The office measures 2,055 square feet and is populated with numerous partition walls and concrete pillars (denoted by black rectangles). For localization experiments, 25 sample locations throughout the office were used. AP locations are denoted by circled numbers.

back to a central server over an Ethernet backhaul. The server then arranges these into groups based on timing and header information to determine which readings belong to the same original transmission. If the server detects that it has received multiple CSI readings from different cards on the same AP, it performs multicard merging as described in §2.1 and replaces them with the merged reading. Upon receiving a CSI reading from an uncalibrated AP, the server initiates the single-packet autocalibration algorithm from §2.2.2, while applying the multipath suppression algorithm (§2.3). After a sufficient number of such packets have been processed for an AP, the system performs the multipacket clustering described in §2.2.3, after which the AP becomes operational.

Replay function. A particular challenge that arises in the evaluation of wireless systems that operate in real-time is the constantly-changing wireless channel. This makes comparisons between two different experimental runs invalid. To combat this issue, we implement a *replay* function which we believe is beneficial not only to Phaser but also to other real-time systems. To accomplish this, Phaser records detailed information about each experiment including packet arrival times, signal amplitude and phase, packet content, and the AP’s calibration data in a log file for replaying purposes. For 30 minutes of real-time experiments with Phaser, the size of the log file is reasonably small: around 100 MB. With this replay function employed, we are able to evaluate different schemes and different parameter settings while keeping the experimental setup and environmental factors unchanged.

4. EVALUATION

Methodology. We experiment in both a busy, uncontrolled 2,055-square foot open-plan office shown in Figure 10 and the controlled anechoic chamber environment of Figure 11. The office is populated with concrete pillars as indicated, as well as numerous wooden partition walls throughout. Co-channel interference and overlapping channel interference are also present in the office. Our APs are mounted near the ceiling, and so the environment is a partial line-of-sight environment: non-line-of-sight when a partition or concrete pillar blocks the mobile’s path to an AP. Because of the firmware limitations mentioned in §3, Phaser on the Intel 5300 NICs can only operate at 5 GHz. As higher-frequency signals are subject to worse



Figure 11: AP (far) and client (near) setup in anechoic chamber with multipath reflector.

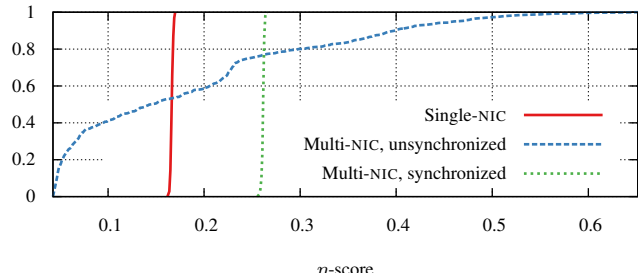


Figure 12: η -scores of a transmitter at 210° with and without multi-NIC operation in an anechoic chamber.

multipath reflections from walls and nearby objects, this carrier frequency is in the most challenging band of the WiFi spectrum.

Evaluation roadmap. We begin with measurements of the accuracy of multicard operation (§4.1) in an anechoic chamber. We then evaluate autocalibration (§4.2) and multipath suppression (§4.3), and report end-to-end results from a localization system built atop Phaser (§4.4), all in the office.

4.1 Multicard operation

In order to test multicard operation in isolation, we perform manual cable calibration on an AP, and place the AP with a client in an interference-free anechoic chamber where the multipath environment can be completely controlled. Our test setup is shown in Figure 11: the metal plate is used to introduce a multipath reflection in later experiments. We average across 1,000 frame transmissions in each experiment.

Line-of-sight. We present data from a single, three-antenna NIC, two three-antenna unsynchronized NICs, and two three-antenna NICs with Phaser’s inter-NIC synchronization (§2.1). Figure 12 shows η -score distributions across frames from each of these three experiments with the client at 210° to the AP’s broadside. Since the experiment took place in a controlled environment, we expect very little variation in the score over time. While this holds for both single-NIC and synchronized multi-NIC operation, we see that for unsynchronized multi-NIC operation, the η -score varies widely across frames as the oscillators of the two cards drift relative to each other. This shows that the multi-NIC synchronization is working correctly; the resulting pseudospectra are stable over time, and more importantly, are of greater fidelity than for a single NIC. We also note that the η -score is higher for multi-NIC operation than single-NIC. This is due to sharper pseudospectra produced as number of antennas increases.

Multipath. Another advantage of a larger array is the ability to resolve multiple arriving signals. Figure 13 shows a similar experi-

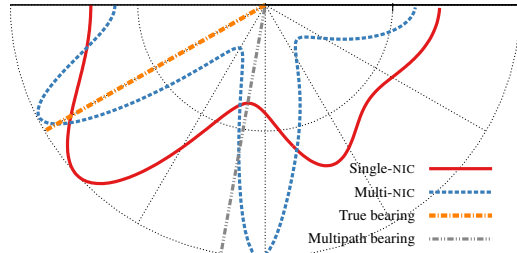


Figure 13: Pseudospectra with a transmitter at 210° and a multipath reflector at 100° from a single-NIC, three-antenna array and a multi-NIC, five-antenna array.

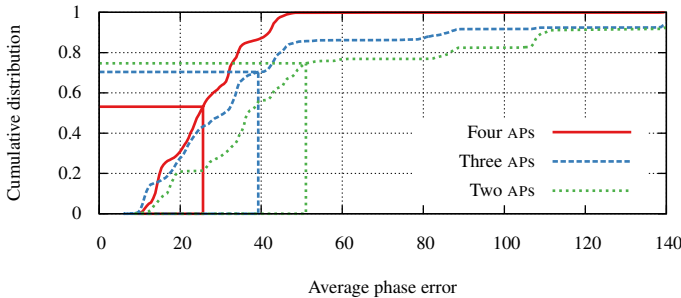


Figure 14: Average single-NIC phase error as the number of calibration transmitters varies. Vertical and horizontal lines denote the mean and the order statistic of the mean respectively.

ment, but with an additional signal arriving at 100° to the array’s broadside. This skews the three-antenna pseudospectrum, whereas the five-antenna pseudospectrum clearly distinguishes the two incoming signals.

4.2 Autocalibration

To evaluate how well autocalibration functions in a real office environment, we place four multi-NIC Phaser APs in the ceiling of our open lab. The true phase offsets were determined by applying manual calibration using an RF signal splitter as described in §2.2.

4.2.1 Number of APs

One of the most important factors for autocalibration is the number of distinct signal sources, as increased path diversity helps eliminate incorrect phase offset combinations caused by persistent multipath fading or interference. In Figure 14, we use this four-AP setup, running autocalibration with differently-sized subsets of APs enabled. Accuracy decreases with transmitter diversity because the clustering at the end of the autocalibration process only works if the true phase offset combination is the only one with samples present in every population. As the number of distinct transmitters decreases, incorrect phase offset combinations are more likely to be present in a sufficient number of populations that they are considered to be more likely candidates than the true phase offset combination. We obtain good calibration accuracy with four, and acceptable accuracy with three active APs.

4.2.2 Sensitivity analysis: Search parameters

In §2.2, we mention a number of parameters that can affect the performance of autocalibration; principally the number of transmitters K , the number of transmissions, and the population size S . In addition, the granularity at which the phase offsets are searched when generating candidate phase combinations, $\Delta\phi$, clearly affects

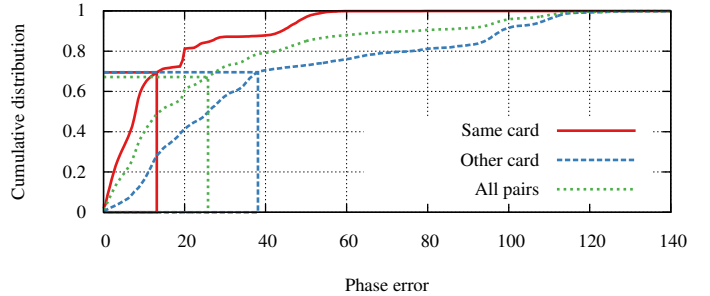


Figure 16: Phase error distribution across antenna pairs for antennas pairs on the same card versus different cards

the accuracy achievable through calibration. Figure 15 shows how modifying each parameter affects the accuracy of autocalibration.

Population size. Recall from §2.2 that population size S determines the number of phase combinations that “survive” each iteration. As S increases, we retain more combinations from each packet, giving the final step of autocalibration and clustering more samples to work with. Results show that increasing the population size S increases the number of samples for the true combination. When we then cluster at the end of the autocalibration process, the cluster near the true combination will have more points, and the end result becomes more accurate.

Step size. The choice of $\Delta\phi$ presents a trade-off between computational cost versus calibration accuracy; as the steps become coarser, the phase difference between the true offsets and their closest step will increase, and so will the overall error. A smaller step size will reduce this quantization error, but will also increase the number of combinations needed for calibration, making it slower. Below a step size of 6° , noise in the calibration process will surpass the step error and we will reach a point of diminishing returns, for both single-NIC and multi-NIC measurements. This correlates well with the lowest observed phase errors across all runs.

Number of frames. We measure the effect of changing the number of frames K that the autocalibration algorithm waits for before performing clustering and picking the final phase offset combination. As this number is lowered, we would expect to see a similar degradation to what is observed as the number of transmitters decreases; fewer samples means incorrect phase offset combinations have a greater chance of creating winning clusters. We observe this trend in Figure 15—as we sample more transmissions, the true phase combinations become more numerous in the final population, and their cluster is more likely to dominate.

Gaussian variance of η -score. Finally, we measure the effect of changing the width of the Gaussian curve that the η -score metric correlates against, as described in §2.2.1. We observe low sensitivity to the width of the Gaussian and good performance at our chosen value ($\sigma^2 = 0.1$).

4.2.3 Phase error and spatial resolution

It is important to make a distinction between phase error and the spatial resolution of the resulting pseudospectra. Though they are both measured in degrees, and a higher phase error will generally cause the resulting pseudospectrum to degrade in quality, there is not a one-to-one correspondence between the two.

To illustrate the impact of phase error on a pseudospectrum, consider Figure 17 where we show a pseudospectrum produced with the correct phase offsets, as well as pseudospectra where each phase offset is perturbed by a random error of $\pm 20 \pm 5$ or $\pm 30 \pm 5$. While

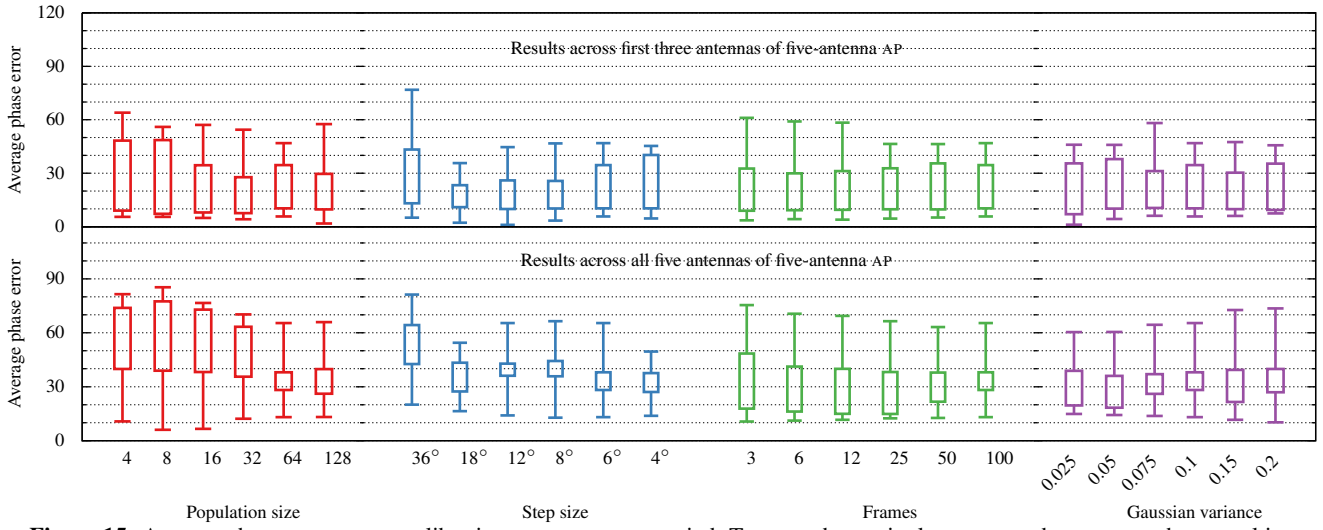


Figure 15: Average phase error as autocalibration parameters are varied. Top row shows single-NIC error, bottom row shows multi-NIC error. The non-variable parameters are held at 64 survivors, 100 packets, 6° step size, and $\sigma^2 = 0.1$. Boxes denote the 25th and 75th order statistics, while whiskers denote the 5th and 95th percentile order statistics. Results are without multipath suppression.

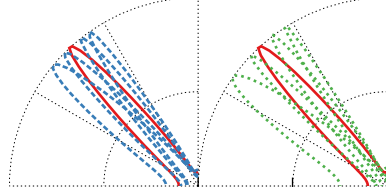


Figure 17: Pseudospectra for varying average phase errors. Solid red line indicates AoA spectrum with perfect calibration. Dashed blue lines (left) show 20° error, dotted green lines (right) show 30° error.

the error is noticeable, the overall shape of the pseudospectrum is maintained even for an average phase error of 30° .

4.2.4 Impact of synchronization on autocalibration

From the lower half of Figure 15, autocalibration accuracy lessens for antennas on a non-primary NIC. By plotting the distribution of absolute phase error for the phase offsets for antennas on the primary NIC and on the secondary NIC separately for a five-antenna, dual-NIC array, we explore the error multi-NIC synchronization introduces.

Figure 16 shows the distribution of phase errors across 700 calibration runs on the four APs in our testbed. The mean phase error increases by almost 20° for the antennas on the secondary NIC. While this is a noticeable error, the fidelity gain from more antennas often outweighs the noise synchronization introduces.

4.3 Multipath suppression

To demonstrate the efficacy of our multipath suppression algorithm, we run the autocalibration algorithm on the same dataset with multipath suppression enabled and disabled. Since the algorithm is non-deterministic, we also run a number of iterations for each configuration. The dataset is the same used for the autocalibration evaluation in §4.2.

Figure 18 shows the calibration error distribution for both versions across all antennas on each AP. Multipath suppression alone reduces the median calibration error from 34° to 24° for multicard operation,

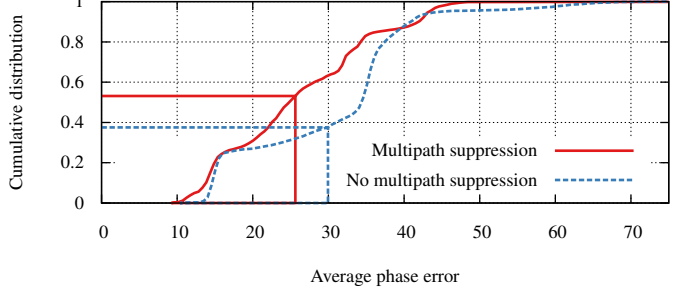


Figure 18: Autocalibration phase error distribution with/without multipath suppression.

and from 12° to 6° for the primary NIC (not shown). We explore the impact of this in the end-to-end evaluation in §4.4.

4.4 Application: Localization

In order to determine whether Phaser truly enables practical phased-array signal processing on commodity hardware, we implement an angle-of-arrival based location tracking system [30] on top of Phaser. In this context, the server constructs pseudospectra from phase-difference information obtained from each AP’s reading in a transmission group and uses this information to triangulate the transmitter’s location. This is done by finding the location on the map that maximizes $\prod_i P_i(\theta_i)$; the combined pseudospectrum probability across APs for the candidate location’s bearing to each AP. All APs in the deployment are first calibrated using autocalibration. Figure 19 shows the end-to-end localization error of this system when deployed on Phaser with four five-antenna APs in our office environment. We also replay the same trace without multipath suppression enabled to evaluate the effect onset detection has on localization accuracy. Results show that Phaser enables practical indoor location estimation on off-the-shelf hardware with little configuration and no training. Multipath suppression further improves mean accuracy by almost a meter, and the 95th-percentile by over two meters. The median accuracy improves by over 50 cm, representing a 35% improvement due to onset detection alone.

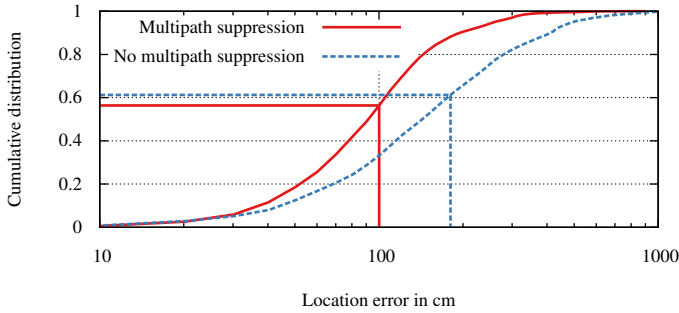


Figure 19: End-to-end localization system error with four multi-NIC five-antenna APs, with and without multipath suppression.

5. RELATED WORK

In this section we survey prior work in location estimation (§5.1), radio imaging (§5.2), and phase calibration (§5.3), and describe how these systems relate to Phaser.

5.1 Indoor location systems

Phaser’s functionality is most directly applicable to indoor location systems, and there are many different such systems.

Ultrasound and light-based methods. Active Badge [28], Bat [29, 11], and Cricket [16] systems are among the pioneers in the ultrasound and ultrasound/RF area, but require specialized hardware and per-room infrastructure. In contrast, localization systems built on top of Phaser are much cheaper and easier to deploy thanks to the ubiquity of wireless APs.

RF-based methods. The RADAR system [3, 4] pioneered this popular approach based on AP radio signal strength maps, with further work refining the approach probabilistically [35], through perturbation [34], and by exploring the use of cross-technology interference [8]. To build the radio map without human involvement, follow-on work uses crowdsourcing, step counting, smartphone inertial sensors [18, 26, 33], and GPS [6]. Other approaches leverage ray tracing [7] or human intervention (either by manual location input [15], or a user’s spinning movement [21]) to obviate the need for manual radio map construction. These RF-based methods, however, often suffer from poor spatial resolution compared to angle-of-arrival based methods.

RF angle-of-arrival based methods. These measure the two-dimensional bearing at which a transmission arrives at the AP [14, 30]. Further work refines these methods to use a smartphone’s inertial sensors to estimate the line-of-sight path to the AP [22], or attempt to isolate the line-of-sight signal in order to decrease the complexity of angle-of-arrival estimation [12]. Phaser’s autocalibration can augment these systems to make them even more practical, and Phaser’s multipath suppression and multicard operation components make them even more functional.

Spot localization. PinLoc [23] places the mobile in one of several pre-defined, geographically separated spots by statistical clustering and classification of 802.11n CSI information. Phaser’s multicard operation can offer these systems the ability to classify based on five or more antennas instead of three, potentially improving system performance.

5.2 Radio imaging

Also known as device-free localization and passive radar, this work uses RF measurements to localize humans and objects moving about in space, without the need for them to be carrying RF transmitters. WiSee [17] uses Doppler shift analysis combined with MIMO spatial

signatures to analyze human motion, and so Phaser’s multi-antenna processing design can complement it. Wi-Vi [2] uses inverse synthetic aperture radar combined with angle-of-arrival measurements using the MUSIC algorithm [20] to track users through walls, and so all three parts of Phaser can add direct benefit.

Other such systems use signal strength and/or Doppler shift measurements only. Ichneea [19] uses statistical processing on received signal strength (RSS) measurements, and MonoStream uses image processing on the magnitude information of 802.11n CSI data to recognize trained patterns when users stand at various locations. Chetty *et al.* [5] describe a single-antenna passive bistatic radar system that can track targets through a wall. Here Phaser is of no immediate benefit, but in general, coherent combination of data from multiple antennas boosts fidelity, and so with this addition, Phaser can offer complementary benefits to these systems.

5.3 Phase calibration

Muti-user MIMO transmit beamforming systems like Argos [24] also need to perform phase calibration. To do so, Argos sends from one antenna on the WARP FPGA-based AP while receiving on the others. But this approach is not directly applicable to current commodity NICs, as they usually do not support transmitting on one antenna while receiving on the other antennas simultaneously. Nevertheless, a similar calibration technique can be applied on APs with multiple NICs; the cards can take turns transmitting and receiving for a brief period after the AP first comes online in order to gather information similar to that obtained in Argos’ calibration phase. However, this calibration technique has a number of drawbacks that make it problematic to use in practice. First, it requires multiple NICs to be present for it to work. As the current trend is for the number of antennas per NIC to increase, the need for multiple NICs is declining, and having a hard requirement on additional hardware for the sole purpose of calibration is undesirable. Second, using an APs own transmissions for calibration means additional shielding is required between the antennas and the antenna ports on the NICs, as any signal leaking between the two will severely skew calibration results. Finally, with dense antenna geometries, and particularly for linear arrays, the antennas themselves will add multipath reflections and obstruct line-of-sight signal propagation, introducing additional errors into the calibration results. Phaser’s autocalibration mechanism is not subject to these problems, but does require cooperation with other APs or mobile clients to function, which is not the case for Argos-like calibration.

6. CONCLUSION

We have described Phaser, a system that allows commodity WiFi APs with or without minor cost-effective hardware modifications to become phased array signal processing platforms capable of high-fidelity array signal processing. Phaser contributes novel design techniques for multi-NIC operation and automatic calibration, and introduces an effective technique for multipath suppression. We have experimentally measured the fidelity of Phaser’s phase measurements, and in an application study we have demonstrated good end-to-end indoor location accuracy. Finally, we have outlined three distinct kinds of wireless systems that benefit from Phaser (§5).

Acknowledgements

The research leading to these results has received funding from the European Research Council under the European Union’s Seventh Framework Programme (FP/2007-2013), ERC Grant Agreement n° 279976. We thank the anonymous reviewers and shepherd for their useful feedback.

7. REFERENCES

- [1] H. Abdel-Nasser, R. Samir, I. Sabek, and M. Youssef. MonoStream: A minimal-hardware high accuracy device-free WLAN localization system. In WCNC, 2013.
- [2] F. Adib and D. Katabi. See through walls with WiFi! In SIGCOMM, 2013.
- [3] P. Bahl and V. Padmanabhan. RADAR: An in-building RF-based user location and tracking system. In INFOCOM, 2000.
- [4] P. Bahl, V. Padmanabhan, and A. Balachandran. Enhancements to the RADAR user location and tracking system. Technical Report MSR-TR-2000-12, 2000.
- [5] K. Chetty, G. Smith, and K. Woodbridge. Through-the-wall sensing of personnel using passive bistatic radar at standoff distances. *IEEE Trans. on Geo. and Remote Sensing*, 50(4):1218–26.
- [6] K. Chintalapudi, A. Iyer, and V. Padmanabhan. Indoor localization without the pain. In *MobiCom*, 2010.
- [7] A. Eleryan, M. Elsabagh, and M. Youssef. AROMA: Automatic generation of radio maps for localization systems. In WINTECH, 2011.
- [8] Y. Gao, J. Niu, R. Zhou, and G. Xing. ZiFind: Exploiting cross-technology interference signatures for energy-efficient indoor localization. In INFOCOM, 2013.
- [9] M. García and C. Oberli. Intercarrier interference in OFDM: A general model for transmissions in mobile environments with imperfect synchronization. *EURASIP Journal on Wireless Communications and Networking*, June 2009.
- [10] D. Halperin, W. Hu, A. Sheth, and D. Wetherall. Tool release: Gathering 802.11n traces with channel state information. SIGCOMM CCR, 41(1), 2011.
- [11] R. Harle and A. Hopper. Deploying and evaluating a location-aware system. In *MobiSys*, 2005.
- [12] D. Inserra and A. Tonello. A frequency-domain los angle-of-arrival estimation approach in multipath channels. *Vehicular Technology, IEEE Transactions on*, 62(6):2812–2818, July 2013.
- [13] T. Laakso, V. Valimaki, M. Karjalainen, and U. Laine. Splitting the unit delay. *IEEE Sig. Proc. Mag.*, 13(1):30–60, 1996.
- [14] D. Niculescu and B. Nath. VOR base stations for indoor 802.11 positioning. In ACM *MobiCom*, 2004.
- [15] J. Park, B. Charrow, D. Curtis, J. Battat, E. Minkov, J. Hicks, S. Teller, and J. Ledlie. Growing an organic indoor location system. In *MobiSys*, 2010.
- [16] N. Priyantha, A. Chakraborty, and H. Balakrishnan. The Cricket location-support system. In *MobiCom*, 2000.
- [17] Q. Pu, S. Gupta, S. Gollakota, and S. Patel. Whole-home gesture recognition using wireless signals. In *MobiCom*, 2013.
- [18] A. Rai, K. Chintalapudi, V. Padmanabhan, and R. Sen. Zee: Zero-effort crowdsourcing for indoor localization. In *MobiCom*, 2012.
- [19] A. Saeed, A. Kosba, and M. Youssef. Ichnaea: A low-overhead robust WLAN device-free passive localization system. *IEEE J. on Sel. Topics in Sig. Proc.*, 8(1), 2014.
- [20] R. Schmidt. Multiple emitter location and signal parameter estimation. *IEEE Trans. on Antennas and Propagation*, AP-34(3):276–80, 1986.
- [21] S. Sen, R. Choudhury, and S. Nelakuditi. SpinLoc: Spin once to know your location. In *HotMobile*, 2012.
- [22] S. Sen, J. Lee, K. Kim, and P. Congdon. Avoiding multipath to revive inbuilding WiFi localization. In *MobiSys*, 2013.
- [23] S. Sen, B. Radunovic, R. Choudhury, and T. Minka. Spot localization using PHY layer information. In *MobiSys*, 2012.
- [24] C. Shepard, H. Yu, N. Anand, L. Li, T. Marzetta, R. Yang, and L. Zhong. Argos: Practical many-antenna base stations. In *MobiCom*, 2012.
- [25] J. K. Tan. An adaptive orthogonal frequency division multiplexing baseband modem for wideband wireless channels. Master’s thesis, Massachusetts Institute of Technology, June 2006. pp. 43–47.
- [26] H. Wang, S. Sen, A. Elgohary, M. Farid, M. Youssef, and R. Choudhury. No need to war drive: Unsupervised indoor localization. In *MobiSys*, 2012.
- [27] J. Wang and D. Katabi. Dude, where’s my card? RFID positioning that works with multipath and non-line of sight. In SIGCOMM, 2013.
- [28] R. Want, A. Hopper, V. Falcao, and J. Gibbons. The active badge location system. *ACM Trans. on Information Systems*, 10(1):91–102, Jan. 1992.
- [29] A. Ward, A. Jones, and A. Hopper. A new location technique for the active office. *IEEE Personal Communications*, 4(5):42–47, Oct. 1997.
- [30] J. Xiong and K. Jamieson. ArrayTrack: A fine-grained indoor location system. In NSDI, 2013.
- [31] J. Xiong and K. Jamieson. Securearray: improving wifi security with fine-grained physical-layer information. In *MobiCom*, 2013.
- [32] Y. Yang, B. Chen, K. Srinivasan, and N. Shroff. Characterizing the achievable throughput in wireless networks with two active rf chains. In INFOCOM, 2014.
- [33] Z. Yang, C. Wu, and Y. Liu. Locating in fingerprint space: Wireless indoor localization with little human intervention. In *MobiCom*, 2012.
- [34] M. Youssef and A. Agrawala. Small-scale compensation for WLAN location determination systems. In WCNC, 2003.
- [35] M. Youssef and A. Agrawala. The Horus WLAN location determination system. In *MobiSys*, 2005.